

A Computational Investigation on Bending Deformation Behavior at Various Deflection Rates for Enhancement of Absorbable Energy in TRIP Steel



HANG THI PHAM and TAKESHI IWAMOTO

Transformation-induced plasticity (TRIP) steel might have a high energy-absorption characteristic because it could possibly consume impact energy by not only plastic deformation but also strain-induced martensitic transformation (SIMT) during deformation. Therefore, TRIP steel is considered to be suitable for automotive structures from the viewpoint of safety. Bending deformation due to buckling is one of the major collapse modes of automotive structures. Thus, an investigation on the bending deformation behavior and energy-absorption characteristic in TRIP steel at high deformation rate is indispensable to clarify the mechanism of better performance. Some past studies have focused on the improvement of mechanical properties by means of SIMT; however, the mechanism through which the energy-absorption characteristic in steel can be improved is still unclear. In this study, the three-point bending deformation behavior of a beam specimen made of type-304 austenitic stainless steel, a kind of TRIP steel, is investigated at various deflection rates by experiments and finite-element simulations based on a constitutive model proposed by one of the authors. After confirming the validity of the computation, the rate-sensitivity of energy absorption from the viewpoint of hardening behavior is examined and the improvement of the energy-absorption characteristic in TRIP steel including its mechanism is discussed.

DOI: 10.1007/s11661-016-3565-9

© The Minerals, Metals & Materials Society and ASM International 2016

I. INTRODUCTION

OVER the last few decades, transformation-induced plasticity (TRIP) steel has attracted the interest of the scientific community.^[1-9] Past studies^[2,10,11] have proven that TRIP steel possesses promising mechanical properties such as high strength, excellent formability, and toughness because of strain-induced martensitic transformation (SIMT). In addition, during the inelastic deformation process of TRIP steel, energy supplied from an external field can be consumed by not only plastic deformation but also transformation to a martensitic phase. At the same time, it is possible that a process of instantaneous deformation such as volume expansion and shape change related to the transformation can dissipate a large amount of energy. As a result, TRIP steel might have an excellent energy-absorption characteristic. Therefore, TRIP steel may be suitable for

automotive structures such as crash boxes, front side members, bumpers, and side panels from the viewpoint of safety.^[12] A dominant mechanism that ensures safety upon collision in automobiles, manufactured using such structures, is buckling. Bending deformation due to buckling is one of the major collapse modes of the automotive structures. In addition, compared with the axial deformation, an experiment for the bending deformation provides more stable results at a structural level. Thus, an investigation on the bending deformation behavior and energy-absorption characteristic of TRIP steel is indispensable to clarify the mechanism that produces better performance.

For understanding the mechanism governing the energy-absorption characteristic during deformation in TRIP steel, it is presumed that SIMT plays a major role in improving the characteristic. However, the SIMT may be suppressed under dynamic loading conditions because of temperature rise in the material due to adiabatic heating by inelastic irreversible work.^[8] At the same time, this heating phenomenon introduces thermal softening of the material. The effect of the amount of transformed martensite on the energy-absorption characteristic in TRIP steel at a high deformation rate seems to be studied insufficiently and the mechanism governing the energy-absorption characteristic is still unclear. The energy absorption of materials can be evaluated from the stress-strain curve obtained by a tensile test. However, at high deformation rate, an interaction between a

HANG THI PHAM, Doctoral Student, is with the Graduate School of Engineering, Hiroshima University, 1-4-1 Kagamiyama, Higashi-Hiroshima, Hiroshima, 739-8527 Japan, and Lecturer with the Faculty of Engineering, Vietnam National University of Agriculture, Ngoxuanquang street, Trauquy, Gialam, Hanoi, 131004 Vietnam. TAKESHI IWAMOTO, Associate Professor, is with the Institute of Engineering, Hiroshima University, 1-4-1 Kagamiyama, Higashi-Hiroshima, Hiroshima, 739-8527 Japan Contact e-mail: iwamoto@mec.hiroshima-u.ac.jp

Manuscript submitted January 20, 2016.

Article published online May 24, 2016

plastic wave and unstable deformation during tension induces difficulties concerning with the onset of necking in a specimen.^[13] Thus, the mechanism governing the energy-absorption characteristic for tensile deformation is quite complicated, especially, at high strain rate.

The bending deformation mode is considered to be quite simple. In fact, large deformation of a smooth beam specimen without such unstable deformation can be obtained under impact bending deformation because the necking cannot be seen in the bending deformation. Thus, a large amount of energy may be dissipated by plastic deformation and phase transformation during the bending deformation of TRIP steel. Moreover, the majority of provided information by the tensile test is about uniform deformation before the onset of necking. Therefore, three-point bending test is conducted for investigation on energy absorption in relatively complicated condition, *i.e.*, non-uniform deformation. Previously, only few studies have focused on the energy-absorption characteristic in TRIP steel. Rong *et al.*^[14] reported that the energy absorption of low-silicon TRIP steel increases with the strain rate; however, the relationship between them is found to be nonlinear based on the results obtained by a tensile test. Curtze *et al.*^[15] showed that the rate sensitivity of the energy-absorption characteristic can be experimentally observed in TRIP steel. Past works^[5,16] explained that the main cause behind the excellent energy-absorption performance of TRIP steel is the considerable amount of martensite formed under dynamic loading. Based on a computational prediction, Zaera *et al.*^[8] indicated that the thermal effects on the energy-absorption characteristic in TRIP steel at high strain rate should be examined. Moreover, Rodríguez-Martínez *et al.*^[17] reported that SIMT is a fundamental contributor to energy absorption in the case of complicated stress states such as a penetration process using a hemispherical projectile. Recently, Zaera *et al.*^[18] showed that energy absorption in TRIP steel decreases under adiabatic conditions because temperature rise suppresses the martensitic transformation.

In this study, the bending deformation behavior of a beam specimen made of type-304 austenitic stainless steel, a kind of TRIP steel, is investigated at various deflection rates. Three-point bending tests are conducted for different levels of the deflection rate at room temperature using an Instron-type conventional material testing machine for quasi-static loading, a drop-weight testing machine, and a testing apparatus based on the split Hopkinson pressure bar (SHPB) method. Computational simulation is performed by the finite-element (FE) method based on the constitutive equations proposed by one of the authors^[19] at the same deflection rate obtained from the experiments. After confirming the validity of the computation, deformation and transformation behaviors under bending deformation are examined at different temperatures. Finally, the mechanism for the energy-absorption characteristic from the viewpoint of hardening behavior in TRIP steel is discussed.

In the following section, detailed experimental procedures for three kinds of bending tests are described.

Then, in Section III, the constitutive equations^[19] proposed in the past, including the transformation kinetics modeled by Iwamoto *et al.*;^[2] the heat conduction equation considering the transformation latent heat^[7] are briefly overviewed. In Section IV, first, the validity of the computation performed in the study is examined by comparing the computational results with the experimental results. Then, the rate sensitivity of energy absorption by means of hardening behavior in TRIP steel is investigated. Next, a computational investigation on energy absorption is conducted at a lower temperature, in which austenite is more unstable. In the final section, the paper is concluded for improvement of the energy-absorption characteristic in TRIP steel.

II. EXPERIMENTAL PROCEDURES

A. Specimen

Beam specimens (length: 100 mm, height: 15 mm, width: 7.5 mm) made of type-304 austenitic stainless steel are used in the present study. The span length is set at 80 mm. After machining, the specimen is subjected to a solution heat treatment at 1323 K (1050 °C) for 30 minutes in an electric furnace (Full-tech FT100) and then quenched in cold water. Finally, a fully austenitic microstructure is obtained.

B. Quasi-Static Bending Test

Quasi-static three-point bending tests are conducted using an Instron-type conventional material testing machine (Shimadzu AG-X250KN). The deflection rate is controlled by using constant crosshead speeds of 0.008, 0.08, 0.8, and 8 mm/second. Displacement of specimen is measured as the displacement of the crosshead of the testing machine and corrected by the values obtained by a laser displacement sensor (Keyence LB-02/LB-62).

C. Drop-Weight Impact Test

In the drop-weight test, a force-sensing block^[20] is placed under the center of the jig to capture the impact force for long time periods by protecting the reflected wave that propagates back into the force-sensing part. The force-sensing block has a small projection, which is used for installing a force sensor. Two rosette strain gages (Kyowa KFG-1-350-D16-11) are glued axisymmetrically at the middle of the projection and connected to a digital oscilloscope (Yokogawa DL-1540) *via* a signal conditioner (Kyowa CDV-700A) through a Wheatstone bridge for amplifying the output voltage signals. In this case, the gages are connected to the bridge box by the four active gage method based on the cancellation of bending deformation in the projection. The output signals obtained with respect to time from this kind of test include oscillations. Thus, a low-pass filter (Nippon Avionics 9B02) with a cut-off frequency of 400 Hz is used. The relationship between the external force values and output signals is determined on the

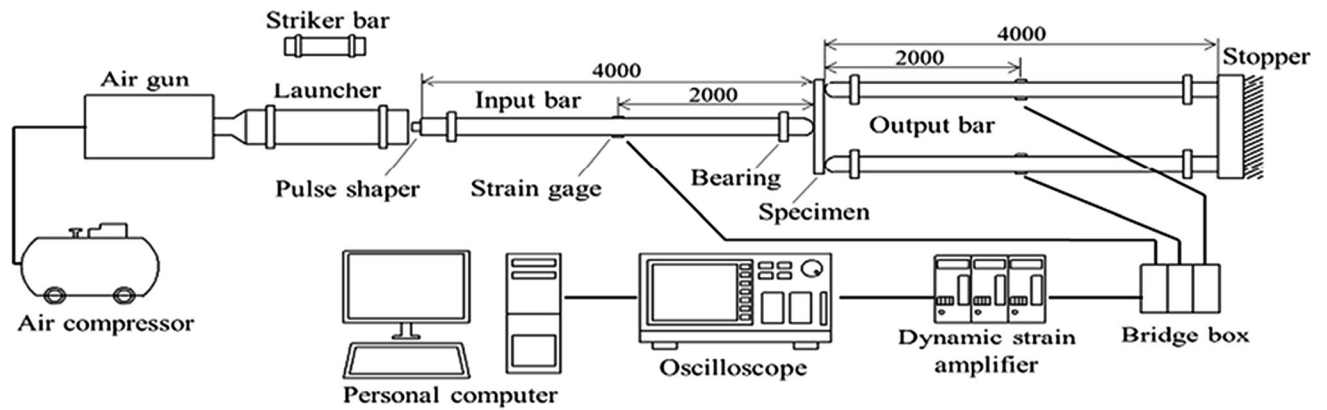


Fig. 1—A schematic of the three-point bending test based on the SHPB method.

basis of a calibration curve obtained using the conventional material testing machine. A weight with a mass of 140 kg is allowed to freely fall from a height of 45 mm. Theoretically, the impact velocity corresponds to 890 mm/second. The velocity of the weight just before it hits the specimen is measured using optical fiber sensors (Keyence FU-77V) and amplifiers (Keyence FS-V31 and 32). Deflection is recorded using a high-speed camera (Photron Fastcam-512PCI32K) during impact deformation with respect to time. A linear magnetic scale system is used to measure the displacement of the weight. The system consists of a magnetic scale (MACOME Laboratory SIS-310S) and a sensor head (MACOME Laboratory SIH-410). When the weight is dropped, the scale moves together with the weight. A digital oscilloscope (Yokogawa DL-2700) acquires the sine and cosine voltage signals output from the sensor head, and the displacement is determined.

D. Impact Test Based on Split Hopkinson Pressure Bar Method

Figure 1 shows the schematic diagram of the modified apparatus for the three-point bending test based on the SHPB method proposed by Yokoyama and Kishida.^[21] The air gun launches the striker bar, which impacts one end of the input bar, by the sudden release of compressed air using a solenoid valve. The specimen is supported by two output bars and subjected to an external force by the input bar. Rosette strain gages (Kyowa KFG-1-350-D16-11) are glued axisymmetrically at the middle position of each pressure bar. The axial strain in the three pressure bars obtained from the gages is recorded using the above-mentioned system. The velocity of the striker bar just before it hits the input bar is measured using the same system mentioned above. A striker bar (length: 500 mm), an input bar (length: 4000 mm), and two output bars (length: 4000 mm) are used. All the pressure bars are 16 mm in diameter. By controlling the pressure in the air tank, the impact velocity of the striker can be controlled. Air pressures of 2 and 5 MPa correspond to impact velocities of 4 and 8 m/second, respectively. To suppress the initial oscillation of the transmitted and reflected stress waves, pulse shapers made of zinc are used. The pulse shapers are

manufactured to be 4 mm in thickness and 6 mm in diameter for an impact velocity of 4 m/second, and 5 mm in thickness and 8 mm in diameter for an impact velocity of 8 m/second. These sizes were determined through some trial and error processes carried out as part of a preliminary study. By using the incident, reflected, and transmitted stress pulses, the deflection at the center of the specimen is measured by the same method with Yokoyama and Kishida.^[21]

E. Input and Output Data of Experiment

In order to investigate the rate-sensitivity of bending deformation behavior for TRIP steel, the displacement-rate is controlled as an input parameter of the test. As above-described, it is controlled by using constant crosshead speeds in quasi-static test, by the height of weight in drop-weight impact test and by the pressure in the air tank of the SHPB method. Thus, it is not any outcomes and not a function of strain. External force and deflection are obtained from the tests as important output data. Of course, the output variables, *i.e.*, force and deflection, depend on stress as well as strain. The deflection is evaluated from the vertical displacement of the middle of lower surface of specimen and its rate is equivalent to the displacement rate. By following the experimental methodology, the reproducibility of the results obtained by quasi-static as well as impact test would be confirmed.

F. Computational Method

The SIMT process itself is quite complicated, and it is hard to clarify the mechanism for improving the characteristics of TRIP steel merely through experiments.^[22] Olson and Cohen^[23] assumed that a mesoscopic shear-band intersection is the dominant mechanism of nucleation in SIMT and formulated a physics-oriented model to precisely predict the temperature-dependent SIMT. Stringfellow *et al.*^[24] incorporated the effect of the mechanical driving force on the martensitic transformation into the model of Olson and Cohen. Tomita and Iwamoto^[7] introduced strain rate sensitivity into the transformation kinetics model proposed by Stringfellow *et al.* Later, Iwamoto *et al.*^[2]

generalized the model by Tomita and Iwamoto to introduce a stress state dependence and formulated a constitutive equation for TRIP steel. The validity of the modeling approach was further investigated^[19,25–30] by comparing the experimental results with those of simulations based on laboratory tests on samples with varying geometries under various loading conditions. More recently, other approaches for the modeling of TRIP steel have been done by many researchers. Mahnken *et al.*^[4] proposed a macroscopic model to simulate the interactive mechanism of phase transformation and plasticity. Kubler *et al.*^[31] introduced a semi-phenomenological model. Recent work done by Fischlschweiger *et al.*^[32] included the effect of back stress into a mean-field model for non-proportional loadings. Here, the model proposed by Iwamoto *et al.*^[2] and Iwamoto and Tsuta^[19] is briefly explained.

G. Multiaxial Constitutive Equation with Transformation Kinetics Model and Heat Conduction Equation for TRIP Steel

The model for the kinetics of SIMT proposed by Iwamoto *et al.*^[2] is employed. The rate of increase in the volume fraction of martensite, \dot{f}' , can be expressed as

$$\dot{f}' = (1 - f') \left(A \dot{\epsilon}_{(\gamma)}^{\text{pslip}} + B \dot{g} \right) \quad [1]$$

$$A = \alpha \eta p n (f^{\text{sb}})^{n-1} (1 - f^{\text{sb}}), \quad B = \eta \frac{dp}{dg} (f^{\text{sb}})^n H(\dot{g}),$$

$$\alpha = \left(\alpha_1 T^2 + \alpha_2 T + \alpha_3 - \alpha_4 \sum \right) \left[\frac{\dot{\epsilon}_{(\gamma)}^{\text{pslip}}}{\dot{\epsilon}_y} \right]^M,$$

$$g = -T + g_1 \sum,$$

where $\dot{\epsilon}_{(\gamma)}^{\text{pslip}}$ is the equivalent plastic strain rate by slip deformation in austenite; f^{sb} is the volume fraction of the shear band; g is the driving force for martensitic transformation; \dot{g} is the rate of the driving force g ; p is the probability that a shear band intersection will act as a nucleation site; $H(\dot{g})$ is the Heaviside step function with respect to \dot{g} , which describes the irreversible process of martensitic transformation; and n and η are geometric constants. α is a parameter related to the stacking fault energy and is a function of the absolute temperature,^[23,24] stress triaxiality parameter Σ ,^[2] and strain rate.^[7] $\alpha_1, \alpha_2, \alpha_3, \alpha_4$ are material parameters, M is the strain rate sensitivity exponent, $\dot{\epsilon}_y$ is the reference strain rate, g_1 is a constant, and T is the absolute temperature. The stress-induced transformation at the nucleation sites can be expressed in terms of B .

According to Iwamoto and Tsuta,^[19] for a large deformation problem, the constitutive equation can be derived as

$$\check{S}_{ij} = \left(D_{ijkl}^v \right) d_{kl} - B_{ij}^e \dot{T} - P_{ij} \Theta_1 - (Q_{ij} - \sigma_{ij}) \Delta v \dot{f}', \quad [2]$$

$$B_{ij}^e = \frac{E}{1 - \nu} \alpha_T \delta_{ij}, \quad P_{ij} = \frac{3E}{2\bar{\sigma}(1 + \nu)} \partial f / \partial \sigma_{ij},$$

$$Q_{ij} = -P_{ij} \sum + \frac{1}{3} \delta_{ij} \frac{E}{1 - 2\nu},$$

where \check{S}_{ij} is the Jaumann rate of Kirchhoff stress S_{ij} ; D_{ijkl}^v is the stiffness tensor after the tangent modulus method^[33] is applied; d_{kl} is the rate of the deformation tensor; B_{ij}^e is a tensor related to the thermal expansion; Δv is the volume change due to phase transformation; σ_{ij} is Cauchy stress; δ_{ij} is Kronecker's delta; α_T is the thermal expansion coefficient; E is Young's modulus; and ν is Poisson's ratio.

Next, the heat conduction equation considering the latent heat because of SIMT^[7] is employed in this study and can be expressed as

$$\rho C \dot{T} = \zeta \sigma_{ij} \dot{\epsilon}_{ij}^p + \kappa^t \nabla^2 T - \rho l_{\alpha'} \dot{f}', \quad [3]$$

where C is the specific heat, ρ is the mass density, ζ is the Taylor–Quinney coefficient, $l_{\alpha'}$ is the latent heat during phase transformation, and κ^t is the thermal conductivity.

According to Tomita and Iwamoto,^[7] the uniaxial stress-strain relationship of a two-phase composite material of austenite including martensite with volume fraction f' has been established in a manner similar to that described by Stringfellow *et al.*^[24] applying Eshelby's solution.^[34] From the self-consistent condition expressed by Stringfellow *et al.*,^[24] the following equation for equivalent stress of the homogenized two-phase composite material can be obtained.

$$\bar{\sigma} = \frac{2}{3} \frac{\dot{\epsilon}^p}{(\dot{\epsilon}_{\alpha'}^p - \dot{\epsilon}_{\gamma}^p)} (\bar{\sigma}_{\gamma} - \bar{\sigma}_{\alpha'}), \quad [4]$$

where $\bar{\sigma}_{\gamma}, \bar{\sigma}_{\alpha'}$ are equivalent stresses of austenite and martensite, respectively. They are dependent on temperature.^[7] $\dot{\epsilon}^p$ is the equivalent plastic strain rate of the composite material. $\dot{\epsilon}_{\alpha'}^p$ and $\dot{\epsilon}_{\gamma}^p$ are equivalent plastic strain rates of martensite and austenite, respectively. Therefore, iso-stress condition is not assumed in this model. In addition, the iso-work condition also is not satisfied.

The uniaxial stress–strain relationship of both phases^[19] is expressed as

$$\bar{\sigma}_{(I)} = \bar{\sigma}_{0(I)} \left[\frac{\dot{\epsilon}_{(I)}^{\text{pslip}}}{\dot{\epsilon}_y} \right]^m, \quad [5]$$

$$\bar{\sigma}_{0(I)} = \sigma_{y(I)} + C_{1(I)} \left\{ 1 - \exp \left(-C_{2(I)} \bar{\sigma}_{(I)}^{\text{pslip}} \right) \right\}^{C_{3(I)}},$$

$$\sigma_{y(I)} = C_{4(I)} \exp(C_{5(I)} T),$$

where I indicates “ γ ” or “ α' ” in the case of austenite and martensite, respectively. $C_{1(I)} - C_{5(I)}$ are material

constants; m is the strain rate sensitivity exponent. The temperature dependence of yield stress also is expressed in this equation.

All these equations are implemented into the FE method. Detailed formulation is provided by the previously published papers.^[7,25] Here, the explanation of procedure is skipped.

H. Three-Dimensional Finite-Element Model, Initial and Boundary Conditions

Figure 2 shows the computational model of the beam specimen in three-dimensional (3D) space. Because of symmetric deformation, the deformation behavior is simulated in one-quarter of the specimen with FE discretization, as shown in this figure. Each hexahedral quadratic element has 20 nodes and eight Gaussian integration points. The nodal displacement rate under the symmetrical boundary condition and at the supporting point is set to be zero. The time history of the nodal deflection rate denoted by $\dot{\delta}$ is set to be constant and is the same as that in the experiment for the

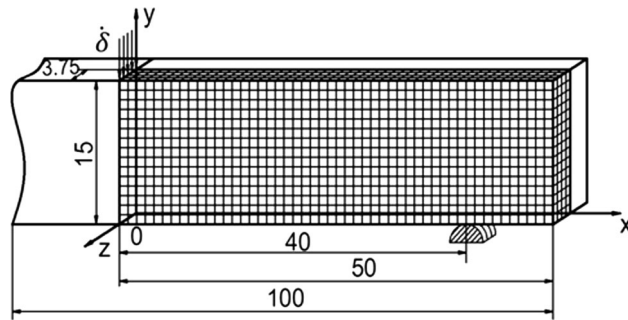


Fig. 2—The FE model of the beam specimen used for 3D computational simulation.

quasi-static condition. Simultaneously, $\dot{\delta}$ for the impact condition is determined from an approximate function of the deflection rate with respect to time obtained from the impact bending tests described in the next section.

According to Iwamoto *et al.*,^[27] based on the method employing a combination between the FE simulation and the nonlinear least-square method with constraint conditions, the parameters in the constitutive equation for TRIP steel have already been identified by using the true stress–plastic strain and the volume fraction of martensite–plastic strain curves obtained from the uniaxial tensile test at different temperatures under isothermal conditions. The parameters and constants of the model applied in this study are shown in Table I.

Since the material used in the present study is the same as that in Reference 19, except for the strain rate sensitivity exponent in Eq. [5], the constants and the material parameters used in the above constitutive equations are the same as those in Reference 19, which were initially identified by Iwamoto *et al.*^[27] The value of the strain rate sensitivity exponent m in Eq. [5] is chosen to be 0.02 in the simulation to have a same response with the experimental result for the both phases at the lowest deflection rate. This value of m is employed for other cases of deflection rate to obtain the actual prediction results. Meanwhile, material parameters used in Eq. [3] are taken from Tomita and Iwamoto.^[7]

I. Input and Output Data of Computation

The deformation rate is also an input data in simulation with value as same with that in experiment. The external force and deflection, which is obtained from the displacement of nodes at the middle of lower surface of specimen, are output data. In addition, volume fraction of martensite calculated from Eq. [1], triaxiality factor, temperature rise, stress and strain

Table I. The Parameters and Constants of the Applied Model^[7,19]

E	Elastic Modulus	193 (GPa)
ν	Poisson's ratio	0.333
m	strain rate sensitivity in Eq. [5]	0.02
$\dot{\epsilon}_y$	reference strain rate in Eqs. [1] and [5]	$5 \times 10^{-4} \text{ s}^{-1}$
α_1, α_2	constant in Eq. [1]	$-2.25 \times 10^{-4}, 4.52 \times 10^{-2}, 11.8, 7.40$
α_3, α_4		
M	strain rate sensitivity in Eq. [1]	0.0013
σ_g	standard deviation in Eq. [1]	129.5
g_o	mean value in Eq. [1]	-87
g_1	constant in Eq. [1]	76.1
n	constant in Eq. [1]	4.5
η	geometrical coefficient in Eq. [1]	14.5
$C_{i(a)}, i = 1-3$	constant in Eq. [5]	2084.2, 0.31, 0.58
$C_{i(a)}, i = 4, 5$	constant in Eq. [5]	1023.9, 0.005
$C_{i(m)}, i = 1-3$	constant in Eq. [5]	1180.7, 17.8, 7.66
$C_{i(m)}, i = 4, 5$	constant in Eq. [5]	1983, 0.0059
ρ	mass density	$0.78 \times 10^4 \text{ (kg/cm}^3\text{)}$
C	specific heat	$0.46 \times 10^3 \text{ (J/(kg K))}$
κ	thermal conductivity	$25.0 \text{ (W/(m}^2 \text{ K))}$
l_{xt}	latent heat	$-1.50 \times 10^4 \text{ (J/kg)}$

tensors as well as their equivalent values at each Gaussian integration point are exported from simulation in order to observe their distribution in the specimen. The volume fraction of martensite and temperature rise is also taken by the volume-average in the entire region of the specimen with respect to deflection level. Furthermore, the computational results in case of without SIMT can be obtained by eliminating the increase in the volume fraction of martensite during plastic deformation in Eq. [1]. However, these data are only observed in computation.

III. RESULTS AND DISCUSSION

A. Experimental Results and Validity of Computational Results

Basically, the values of external force and deflection obtained from three-point bending test change for different sizes of specimen. However, a similar phenomenon in rate-sensitivity of deformation behavior could be captured. In order to eliminate the size effect of specimen and obtain the force-deflection curve, the external force and the deflection are normalized. Moreover, it is necessary to normalize values of deflection to evaluate how the deformation level of specimen is. According to this process, the obtained results can be much more general. A measured or computed external force P is normalized as the ratio of the maximum bending stress at the middle of the specimen to the temperature-dependent initial yield stress σ_y calculated by Eq. [5] and is expressed as

$$P_n = \frac{PL}{4Z\sigma_y(T)}, \quad [6]$$

where L is the span length and Z is the section modulus.

The normalized deflection is calculated based on value of the maximum bending strain in the case that the shape of the deformed specimen is assumed to be an arc. The normalized deflection δ_n and the deflection rate $\dot{\delta}_n$ are calculated as

$$\delta_n = 4h\delta/L^2, \quad \dot{\delta}_n = 4h\dot{\delta}/L^2, \quad [7]$$

where h is the height of the specimen and δ and $\dot{\delta}$ are obtained deflection and the deflection rate, respectively. Detailed idea of this normalization is given in Appendix A. Additionally, in order to distinguish the experimental and simulation results, the label “Exp” and “Sim” will be shown in following figures to express for results obtained from experiment and computation, respectively.

Figure 3 shows a comparison between input and output force of the impact test based on SHPB method with impact velocity of (a) 4 m/s and (b) 8 m/s. From this figure, the dynamic force equilibrium between input and output forces could be confirmed.

In the quasi-static tests, the rate of deformation remains roughly unchanged in terms of time. In the drop-weight test, the deflection rate can be determined from the results obtained using the high-speed camera and those obtained using the linear magnetic scale. The deflection rate for the impact test based on the SHPB technique can be calculated by using the stress waves. Figure 4 shows the normalized deflection rate with respect to time obtained from the three impact tests in experiment. From this figure, the maximum normalized deflection rate is approximately 8, 40, and 80 s^{-1} for the impact deformation. Meanwhile, the corresponding normalized deflection rate is approximately 8×10^{-5} , 8×10^{-4} , 8×10^{-3} , and $8 \times 10^{-2} s^{-1}$ for the quasi-static deformation. These values of the deflection rate are used as representative values.

Figure 5 shows the normalized external force–normalized deflection curves obtained from both the experiment and computational simulations for various normalized deflection rates at room temperature. A fairly good agreement between the computational and experimental results can be seen in the range of the normalized deflection rate from 8×10^{-4} to $8 s^{-1}$. At the same time, the values for the numerical simulation under the impact tests at normalized deflection rates of 40 and 80 s^{-1} are different from those for the experiment in the early stage of the deformation. This difference is induced by an intrinsic oscillation of the specimen during the impact bending deformation. Moreover, the relatively gentle incident wave generated by using the pulse shaper is still slightly steep and the oscillation is

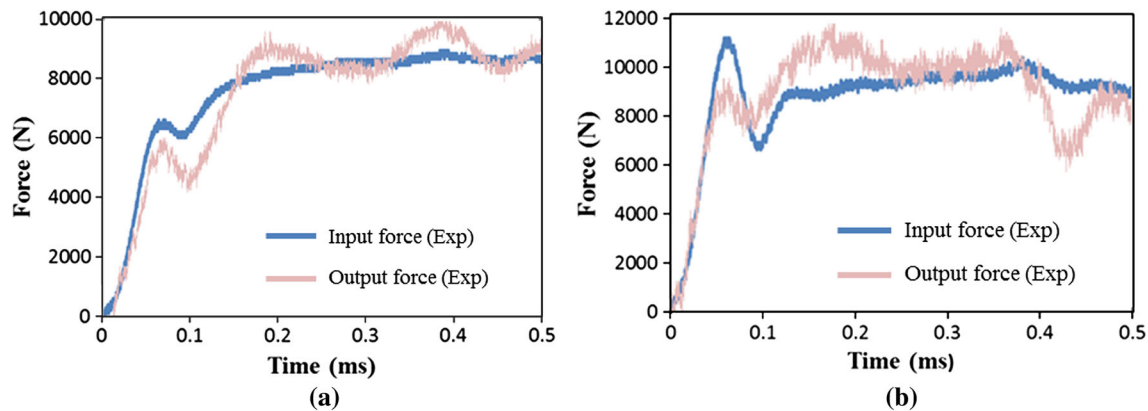


Fig. 3—Input and output force of the impact test based on SHPB method with impact velocity of (a) 4 m/s and (b) 8 m/s.

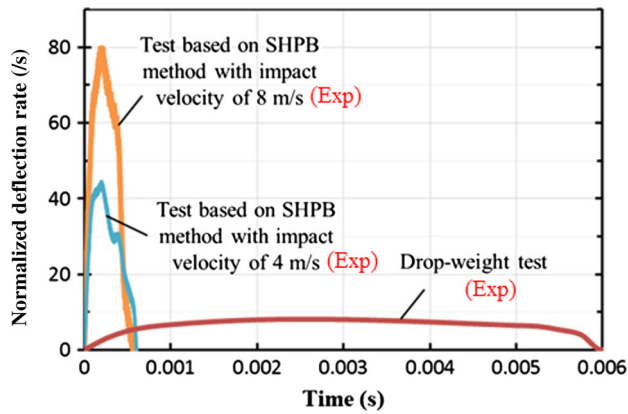


Fig. 4—Normalized deflection rate-time curves obtained from the impact tests in experiment.

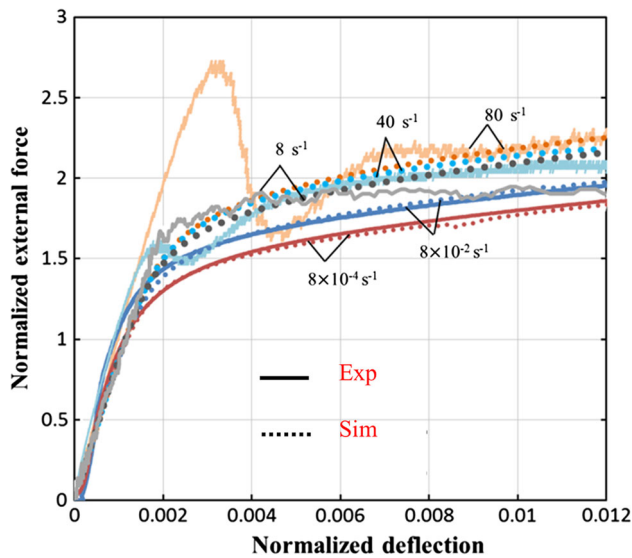


Fig. 5—Normalized external force-normalized deflection curves obtained from the experiment and FE simulation for various normalized deflection rate at room temperature.

suppressed insufficiently. However, in the stage of the larger deformation, the forces gradually approach each other. Finally, a fairly good agreement is observed. Thus, it is obvious that the difference between experiment and simulation is not only deterministically but also statistically small. As a result, it can be said that the validity of the computational results is confirmed.

Figure 6 shows the relationship between the normalized external force and the normalized deflection rate for the normalized deflections of 0.006 and 0.011 in a semi-logarithmic plot. The normalized external force gets higher at higher normalized deflection rate. A positive rate sensitivity of normalized external force can be observed from quasi-static to impact deformation. At both levels of normalized deflection, the linear relationship between the normalized external force and normalized deflection rate in the cases of the quasi-static condition can be seen. The slope of this relationship is

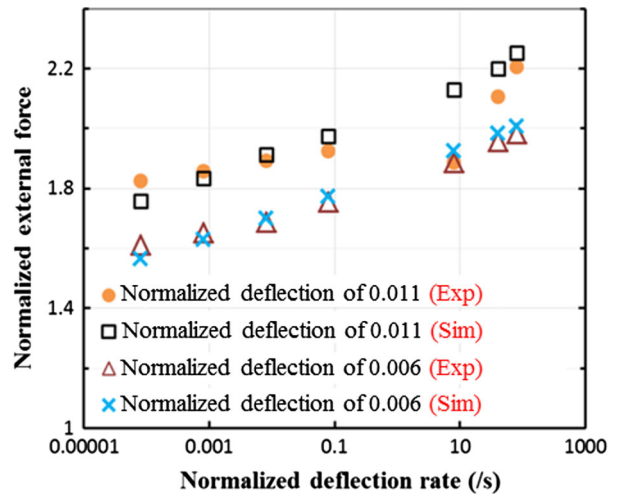


Fig. 6—A plot of the normalized external force with respect to the normalized deflection rate for a normalized deflection of 0.006 and 0.011.

slightly larger in the impact condition. As a result, this relationship becomes nonlinear.

B. Mechanism of Energy Absorption by Computational Simulation at Room Temperature

In this study, the three-point bending test on smooth specimen without fracture and necking is conducted to investigate energy-absorption characteristic for TRIP steel. As similar to the Charpy impact test, it is common to determine energy absorption on the basis of the area surrounding a force–deflection curve until maximum deflection at fracture. In the case of a use of the smooth specimen, there is quite high possibility not to show the fracture because of high ductility in TRIP steel. This means the maximum deflection should be introduced from the other criteria. Here, energy absorption is just evaluated in terms of the increase in the normalized external force because the area surrounding the normalized force–normalized deflection curve increases until a certain level of normalized deflection. From Figures 5 and 6, TRIP steel might have a higher energy-absorption characteristic at a higher deflection rate from the viewpoint of the hardening effect including thermal softening effect. Additionally, a positive rate sensitivity of energy absorption in TRIP steel is clearly observed from quasi-static to impact deformation. From this point of view, TRIP steel might show excellent energy-absorption performance under impact loading because more energy might be consumed by inelastic deformation process for higher deflection rate. This phenomenon can be explained from three viewpoints of effects of transformation strain, work-hardening, rate-sensitive hardening, and thermal softening of austenite and martensite.

In order to confirm the effect of hardening behavior in martensite and transformation strain, the formation of martensite during bending deformation in TRIP steel at room temperature in the specimen is investigated and the influence of SIMT on the bending deformation

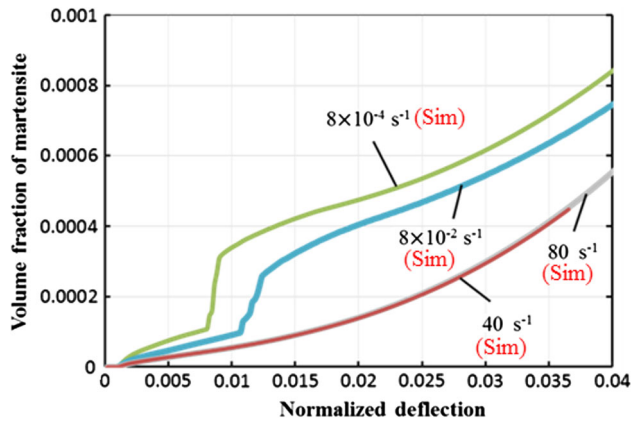


Fig. 7—The volume fraction of martensite in the specimen with respect to normalized deflection for various normalized deflection rate obtained from simulation.

behavior and energy absorption is discussed from the viewpoint of enhancement of hardening. Figure 7 shows the volume fraction of martensite plotted as a function of the normalized deflection for different normalized deflection rates at room temperature obtained from simulation. Here, it is noted that the volume-average in the entire region of the specimen is taken on the volume fraction of martensite. This is why the value of vertical axis is quite small because of the non-uniform deformation. Since the validity of the transformation kinetics model employed in the present study has already been confirmed by some past studies,^[2,19,22,29] the results about volume fraction of martensite, which are computationally calculated by Eq. [1] with respected to plastic deformation in this figure, could be valid. In this figure, the results of highest normalized deflection rate we investigated, $8 \times 10^{-2} \text{ s}^{-1}$ in quasi-static test and much lower normalized deflection rate, $8 \times 10^{-4} \text{ s}^{-1}$ are shown in order to compare clearly with the results in impact test. Totally, the rate-sensitivity of volume fraction of martensite and its effects on the performance of TRIP steel can be discussed. From this figure, the value of volume fraction of martensite is quite low especially at high normalized deflection rate. Moreover, there is almost zero difference between the results of the normalized volume fraction of martensite for the normalized deflection rates of 40 and 80 s^{-1} . On the other hand, the value of SIMT is expected to continuously increase with an increase in deformation since the saturation of SIMT is not be seen at this level of normalized deflection.

Figure 8 presents the normalized external force–normalized deflection relationship for normalized deflection rates of 8×10^{-4} and 8×10^{-2} in quasi-static and 80 s^{-1} in impact condition with and without the consideration of SIMT at room temperature obtained from simulation. From this figure, at larger normalized deflection, a higher value of normalized force is shown in TRIP steel with SIMT for the cases of low normalized deflection rate, whereas the difference cannot be seen for 80 s^{-1} at this level of normalized deflection in the steel with and without SIMT. Although the difference in the

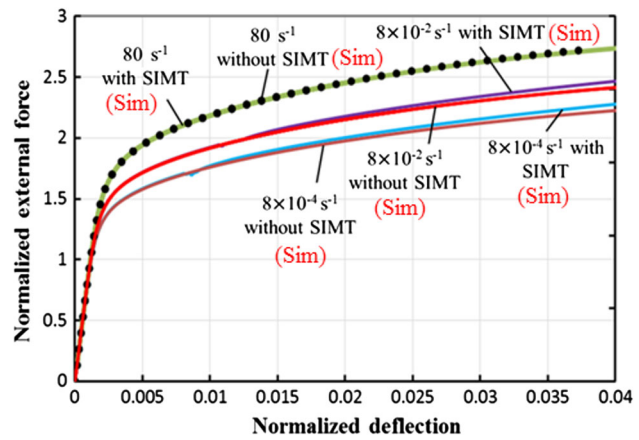


Fig. 8—The relationship between the normalized external force and normalized deflection for three normalized deflection rates with and without the consideration of the effect of the SIMT obtained from simulation.

cases with and without SIMT might be experimentally observed, it is quite difficult to measure the volume fraction of martensite in the entire region of the specimen as well as its local value and other physical variables, which affect the SIMT, with respected to deformation level in experiment. Meanwhile, since the applied model is confirmed by some past studies^[2,19,22,29] and the computation is confirmed by a fairly good correspondences as above-discussed, the difference in the cases with and without SIMT in this figure could be validated. Consequently, influence of SIMT in TRIP steel is only discussed by computational results and an experimental observation seems to be really limited. From the viewpoint of hardening, the effect of SIMT on energy-absorption characteristic cannot be obviously observed at room temperature at this level of normalized deflection for 80 s^{-1} . In the case of high normalized deflection rate, a quite small volume fraction of martensite cannot be responsible for high performance of TRIP steel because of the stability of the parent phase at room temperature as well as the high temperature rise as can be seen in Figure 7. This observation agrees with the result of Zeara *et al.*^[18] which showed that the martensitic transformation does not improve energy absorption at sufficient high strain rate. This result is indicated only for investigated steel of grade as type-304 austenitic stainless steel. However, for other kind of TRIP steel with more unstable austenite, for example, type-301 austenitic stainless steel, it is expected that a considerable amount of SIMT is transformed at room temperature.^[35] Thus, the effect of SIMT on the energy-absorption characteristic at high deformation rate might be seen more clearly. The mechanism for energy absorption at room temperature in TRIP steel with more unstable parent phase needs to be investigated. It is considered that a large amount of the martensitic phase may be transformed as the test temperature decreases because this would decrease the stability of the parent phase. In order to clarify the mechanism for energy absorption in the steel with the effect of SIMT, energy absorption should be

investigated at lower test temperature. Through the investigation on energy-absorption characteristic of the grade of investigated steel at lower temperature, the mechanism for other kind of TRIP steel with lower stability in austenite at room temperature, for example, type-301 austenitic stainless steel, can be understood. Moreover, based on the results for type-304 austenitic stainless steel at lower temperature, it might help for a choice the grade of TRIP steel or control the chemical composition of TRIP steel to improve energy absorption.

C. Discussion on Energy Absorption at Lower Temperature Where Lower Stability in Austenite

Next, the formation of martensite and effect of SIMT on energy-absorption characteristic at 80 K ($-193\text{ }^{\circ}\text{C}$), where it seems that the effects can be clearly expected, is discussed. Figure 9 shows the volume fraction of martensite in the specimen with respect to normalized deflection for different normalized deflection rates at 80 K ($-193\text{ }^{\circ}\text{C}$) obtained from simulation. Also, the volume-average in the entire region of the specimen is taken on the volume fraction of martensite. Thus, the value of vertical axis is still small. A considerably higher value of the normalized volume fraction of martensite can be observed at 80 K ($-193\text{ }^{\circ}\text{C}$) than that at 298 K ($25\text{ }^{\circ}\text{C}$), especially at 40 and 80 s^{-1} . At higher deformation rate, volume fraction of martensite in the entire region of the specimen is higher. Noticeably, the saturation of volume fraction of martensite is not observed in both cases of investigated normalized deflection rate. This phenomenon is totally different from the results of tensile tests in Reference 7, which shows a saturation of SIMT in the early stage of deformation at 80 K ($-193\text{ }^{\circ}\text{C}$), especially at high strain rate. According to Tomita and Iwamoto,^[7] with the saturation of the volume fraction of martensite with an increase in deformation, the ductility can be reduced. The continuous formation of martensite with an increase in the deformation, especially in the region of

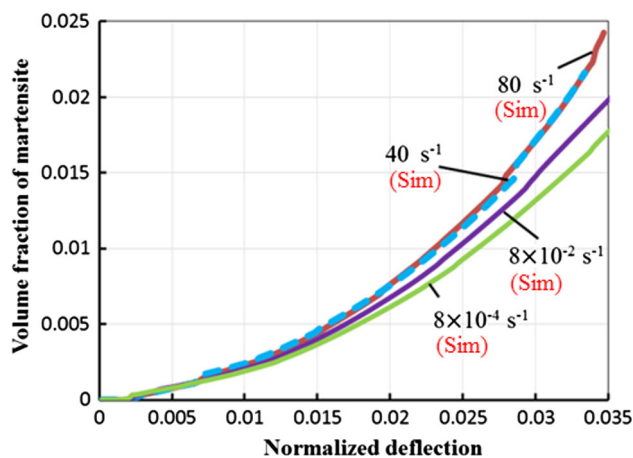


Fig. 9—The volume fraction of martensite in the specimen with respect to normalized deflection for different normalized deflection rates at 80 K ($-193\text{ }^{\circ}\text{C}$) obtained from simulation.

uniaxial tension, is the most important factor for improving ductility.

The relationship between normalized external force and normalized deflection for different normalized deflection rates with and without the consideration of the SIMT at 80 K ($-193\text{ }^{\circ}\text{C}$) obtained from simulation is shown in Figure 10. At the same normalized deflection, the steel with SIMT shows higher external force for all cases of normalized deflection rate investigated. A considerable effect of SIMT on the increase in the force, which cannot be seen at room temperature, is presented in this figure. This might be derived from a large amount of martensite transformed at low temperature. On the other hand, from this figure, it can be considered that a drop of normalized external force can be seen because of extremely high plastic strain near the loading point at high deformation rate. Especially, this phenomenon is observed in earlier stage in the material without SIMT. Next, the deformation behavior of the steel is examined at normalized deflection of 0.02 in detail.

In order to clearly observe the improvement of normalized force because of SIMT, Figure 11 shows the relationship between the difference of normalized force from the result without SIMT at the normalized deflection of 0.02 and the normalized deflection rate in a semi-logarithmic plot obtained from simulation. The value of vertical axis is the increase in normalized external force because of SIMT normalized by the obtained value at $8 \times 10^{-4}\text{ s}^{-1}$. From this figure, the difference of normalized external force is larger at higher normalized deflection rate. Noticeably, the value for cases of 40 and 80 s^{-1} is almost 1.5 times as much as it for case of $8 \times 10^{-4}\text{ s}^{-1}$. Therefore, under the condition of low stable parent phase, the SIMT is more effective at higher rate of deformation as shown in Figure 9. This can be explained by not only the formation of more shear-band intersections but also the higher probability for a high rate of deformation at a low environmental temperature, as expressed in Eq. [1].^[7] As previously mentioned, energy absorption in TRIP steel is evaluated in terms of the increase in the normalized external force. Thus, at 80 K

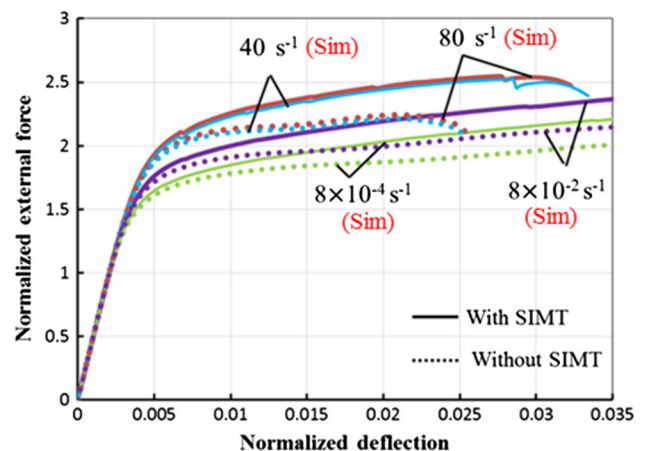


Fig. 10—The relationship between the normalized external force and normalized deflection for different normalized deflection rates at 80 K ($-193\text{ }^{\circ}\text{C}$) with and without the consideration of the effect of SIMT obtained from simulation.

(−193 °C), energy-absorption characteristic is considered to be clearly improved because of SIMT for all cases of investigated normalized deflection rate.

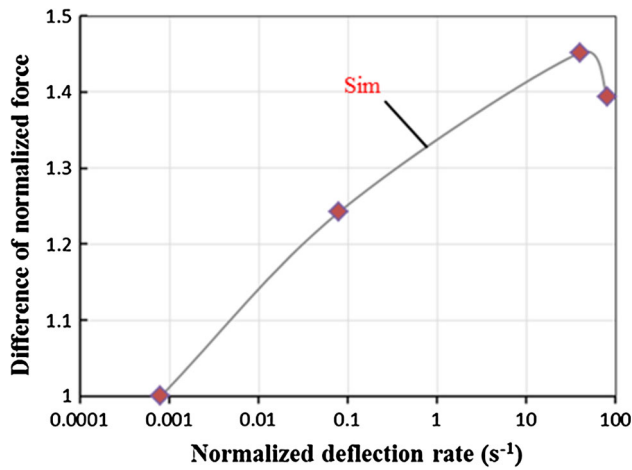


Fig. 11—The relationship between the difference of normalized force from the result without SIMT at the normalized deflections of 0.02 and the normalized deflection rate in a semi-logarithmic plot obtained from simulation.

Figure 12 shows the distribution of volume fraction of martensite in the specimen for normalized deflection rate of (a) 8×10^{-4} and (b) 80 s^{-1} and a normalized deflection of 0.02 obtained from simulation. In general, for both cases of normalized deflection rate, the volume fraction of martensite distributes in the region near the loading point and on the lower side of specimen. A considerably large amount of SIMT can be observed near the loading point. At higher normalized deflection rate of 80 s^{-1} , slightly higher amount of martensite on the lower side of specimen can be observed compared to that at $8 \times 10^{-4} \text{ s}^{-1}$. It seems that SIMT is more favorable for the case of higher deformation rate.

The distribution of physical variables is examined for discussions on the effect of SIMT. Figure 13 shows the distribution of triaxiality factor in the specimen for normalized deflection rate of (a) 8×10^{-4} and (b) 80 s^{-1} and a normalized deflection of 0.02 obtained from simulation. A non-uniform distribution of the triaxiality factor can be observed. In particular, the triaxiality factor clearly distributes separated regions with its lower, higher, and zero values, which correspond to uniaxial compression, uniaxial tension, and simple shear, respectively. Noticeably, a small region of tensile stress state with a considerably high value of triaxiality

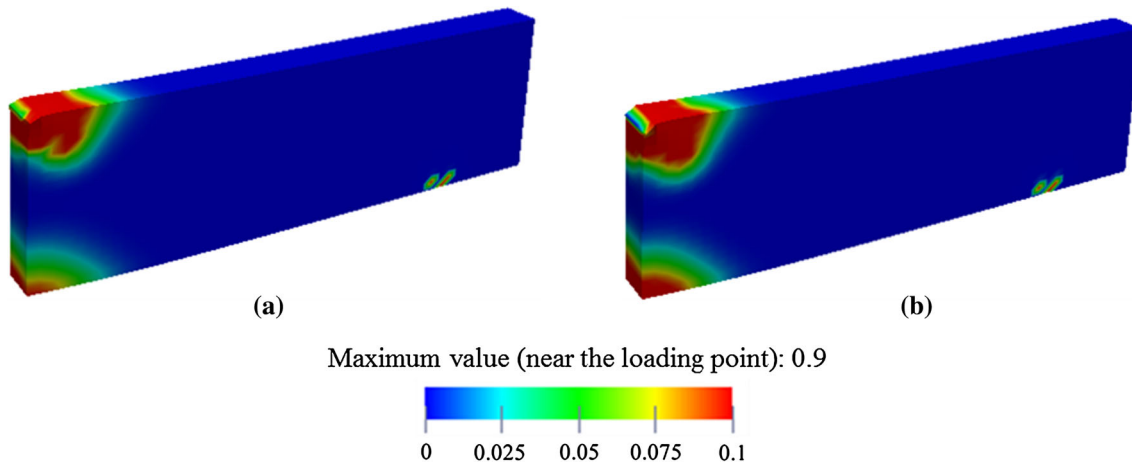


Fig. 12—The distribution of volume fraction of martensite for normalized deflection rate of (a) 8×10^{-4} and (b) 80 s^{-1} at a normalized deflection of 0.02 obtained from simulation.

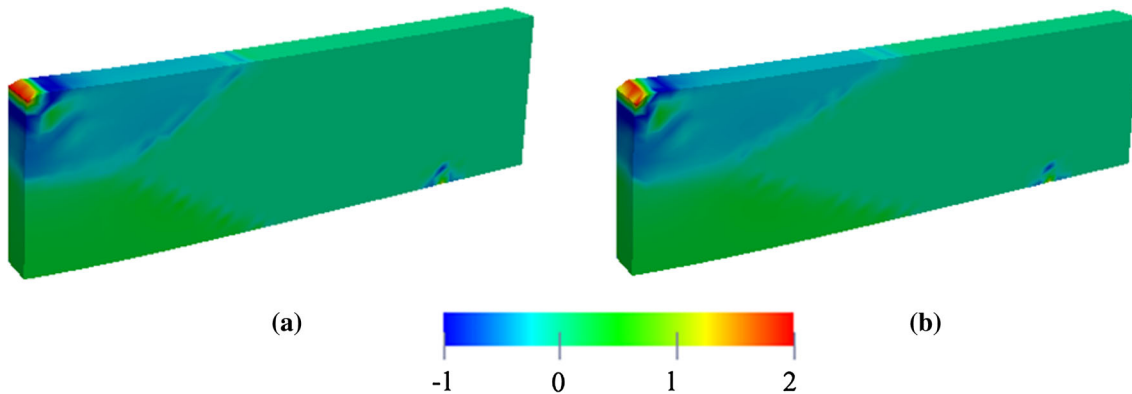


Fig. 13—The distribution of triaxiality factor in specimen for normalized deflection rate of (a) 8×10^{-4} and (b) 80 s^{-1} at a normalized deflection of 0.02 obtained from simulation.

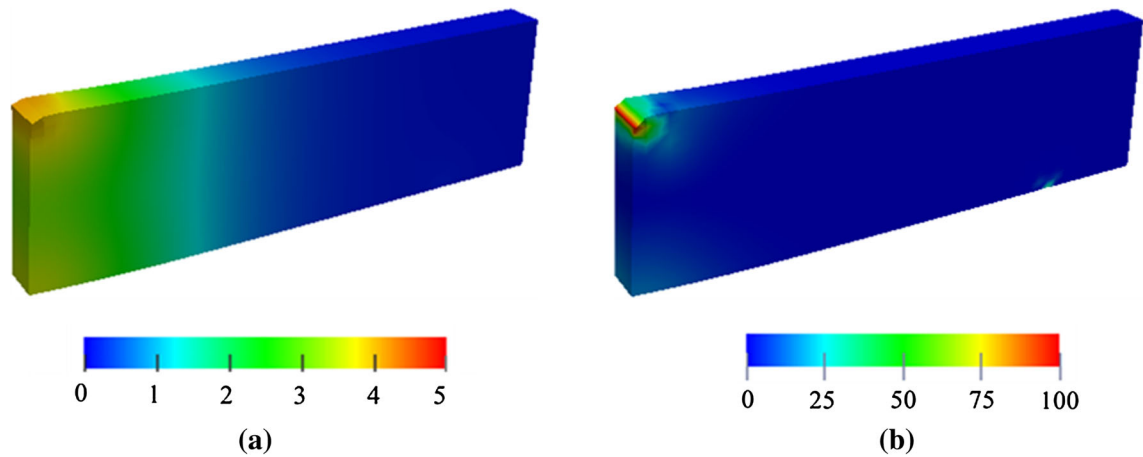


Fig. 14—The distribution of temperature rise T (K) in the specimen for normalized deflection rate of (a) 8×10^{-4} and (b) 80 s^{-1} and a normalized deflection of 0.02 obtained from simulation.

factor is seen near the loading point. Moreover, at higher normalized deflection rate, the region of simple shear is smaller because of an extension of the both regions with uniaxial compressive and tensile stress state. At higher level of deformation, the regions with uniaxial compressive and tensile stress state are expected to be expanded.

Figure 14 shows the distribution of temperature rise in the specimen for normalized deflection rate of (a) 8×10^{-4} and (b) 80 s^{-1} at a normalized deflection of 0.02 obtained from simulation. A low temperature rise, just about 5 K as a maximum, is distributed in a larger region near the loading point at $8 \times 10^{-4} \text{ s}^{-1}$. At this normalized deflection rate, almost uniform distribution of temperature rise can be observed, whereas Figure 14(b) shows a significantly higher temperature rise concentrated near the loading point at 80 s^{-1} . The region of high temperature rise gets smaller at higher normalized deflection rate. It can be considered that the rate of deformation is higher than the rate of diffusion of temperature at higher normalized deflection rate. Therefore, it is quite easier that the temperature diffuses and transfers from the surface in larger region at $8 \times 10^{-4} \text{ s}^{-1}$ compared to the case of 80 s^{-1} . As a result, the size of the region of higher temperature rise strongly depends on the rate of deformation. On the other hand, a high temperature rise at 80 s^{-1} might attribute the distribution of SIMT near the loading point. However, at 80 K ($-193 \text{ }^\circ\text{C}$), the temperature is still sufficiently low and belongs to the region ranging from M_S to M_d . It means that the suppression of SIMT because of a high temperature rise in this condition can be neglected. Additionally, the influence of high temperature rise on the SIMT can be seen only in a small region near the loading point because of the local distribution of high temperature rise at high rate of deformation. In the region encompassing the region of relatively high temperature rise and on the lower side of specimen, effect of high temperature rise on transformation site as well as the probability of martensitic transformation is small. Therefore, at 80 K ($-193 \text{ }^\circ\text{C}$), a considerable amount of martensite is transformed in

these regions as shown in Figure 12. It is considered that, at higher deformation, volume fraction of martensite in case of high deflection rate continuously increases because of an extension of the regions with uniaxial compressive and tensile stress state and the concentration of high temperature rise. This can explain for the result in Figure 9 where the saturation of volume fraction of martensite cannot be seen.

At the discussion on Figure 10, the drop in the force can be observed and the drop for the case without SIMT can be observed earlier than the case with SIMT. It can be considered that this phenomenon is used as a criterion to evaluate ductility. Thus, the discussion of the energy absorption can be made from the viewpoints of both strength and ductility. Figure 15(a) shows a schematic of whole specimen with the applied load. A symbol-like human eye is inserted into this figure to indicate direction of observation for Figure 15(b). Figure 15(b) shows a quarter of upper surface of specimen which is denoted by the hatch in Figure 15(a) obtained by experiment after finishing deformation at normalized deflection of 80 s^{-1} at room temperature. It can be clearly seen from this figure that the thickness of specimen around the loading point is considerably changed and the sharp edge can be observed in the left lower part of the figure.

Figure 16 shows the distribution of (a) equivalent plastic strain, (b) normalized plastic strain rate and (c) normalized equivalent stress for the steel with and without SIMT in simulation for normalized deflection rate of 80 s^{-1} at a normalized deflection of 0.02 obtained from simulation. This figure shows the upper surface of specimen observed from the top view as same as Figure 15(b). Here, the equivalent stress is normalized by yield stress and plastic strain rate is normalized by given deflection rate. Since the level of deformation and testing temperature in experiment and simulation in this figure are different, the profile of specimen in experiment obviously differs from that in computation. However, a considerable change in the thickness of specimen around the loading point is also observed in simulation. This means that the specimen is deformed locally in

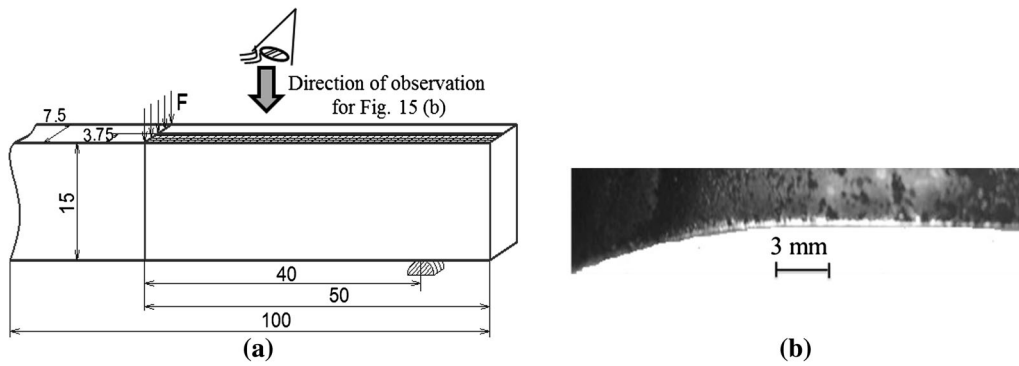


Fig. 15—(a) A schematic of whole specimen with the applied load and (b) a quarter of upper surface of specimen which is denoted by the hatch in (a) obtained by experiment after finishing deformation at normalized deflection of 80 s^{-1} at room temperature.

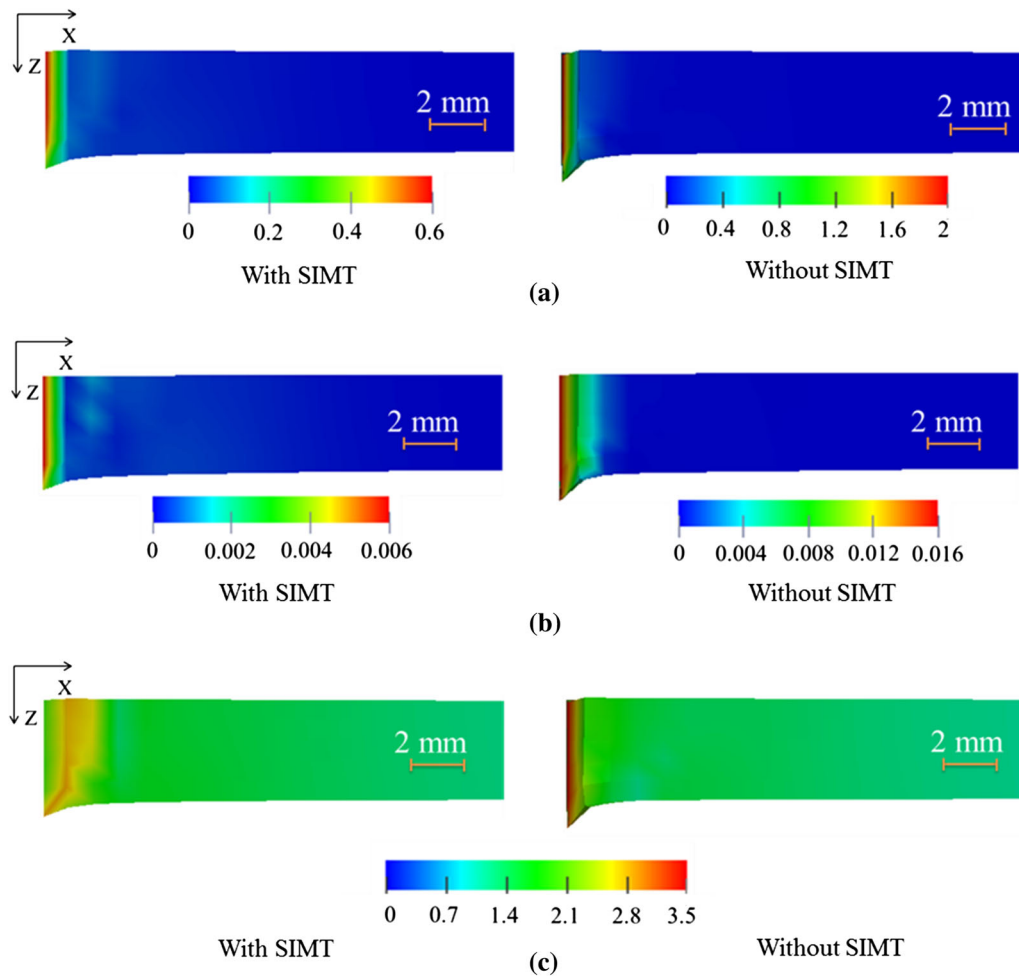


Fig. 16—The distribution of (a) equivalent plastic strain, (b) normalized plastic strain rate and (c) normalized equivalent stress for the steel with and without SIMT in simulation for normalized deflection rate of 80 s^{-1} at a normalized deflection of 0.02 from the top view obtained from simulation.

thickness-direction near the loading point. This phenomenon might come from the tensile stress state with high value in this region as shown in Figure 13 as well as the concentration of relatively high temperature at 80 s^{-1} . Obviously, the maximum value of equivalent plastic strain and normalized plastic strain rate contributes around the loading point. Compared to the case

with SIMT, the steel without SIMT shows higher maximum equivalent plastic strain and normalized plastic strain rate at normalized deflection of 0.02. A strong localized deformation in thickness-direction can induce such extremely severe deformation near the loading point and a fracture will appear at a sufficient equivalent plastic strain. Moreover, from Figure 16(c), maximum

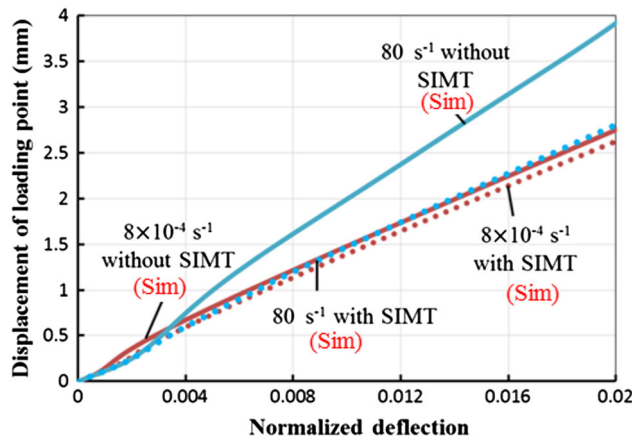


Fig. 17—The relationship between the displacement of the loading point and normalized deflection in the steel with and without SIMT for normalized deflection rate of 8×10^{-4} and 80 s^{-1} obtained from simulation.

equivalent stress distributes near the loading point and it becomes much higher for the case without SIMT. It is expected that the fracture will occur earlier in the steel without SIMT because of higher value of maximum equivalent plastic strain, normalized plastic strain rate as well as equivalent stress at normalized deflection of 0.02.

Figure 17 shows the vertical displacement at the loading point with respect to the normalized deflection with and without SIMT for normalized deflection rate of 8×10^{-4} and 80 s^{-1} obtained from simulation. In the cases without SIMT, the displacement at the loading point is larger at higher rate of deformation. This can be explained that a localization of deformation is induced near the loading point because of thermal softening effect due to a relatively high temperature rise at 80 s^{-1} . On the other hand, at the same normalized deflection rate, the steel with SIMT indicates considerably lower displacement compared to the steel without SIMT, especially at 80 s^{-1} . This can attribute the lower value of equivalent plastic strain and normalized plastic strain rate near the loading point with the consideration of SIMT in Figure 16. The formation of hard martensitic phase near the loading point at 80 s^{-1} might increase the strain hardening of material in this region. Therefore, the localization of deformation in loading direction is retarded because of SIMT. From this phenomenon, the distribution of volume fraction of martensite becomes quite important and should be noticeable.

From the Figures 16 and 17, a strong localization near the loading point at 80 K ($-193 \text{ }^\circ\text{C}$) because of a concentration of relatively high temperature rise might induce a crashed element in simulation and then leads a drop in force. Therefore, the phenomenon of the drop in force in Figure 10 at high deflection rate is strongly related to the fracture and considered as a criterion for discussion of ductility of the material. The distribution of a large amount of martensite near the loading point in Figure 12 delays the drop in force in the steel with SIMT. This means that a fracture in specimen might appear at larger level of deformation. From this viewpoint, the ductility of TRIP steel might be enhanced

in three-point bending deformation because of SIMT as well as the strain rate hardening effect. As a result, it is inferred that the ductility of TRIP steel at a high deformation rate is enhanced because of SIMT, leading an improvement of energy absorption. Based on the results at low test temperature, the mechanism for energy absorption in the TRIP steel with more unstable austenite, for example, type-301 austenite stainless steel, at room temperature can be clarified.

IV. CONCLUDING REMARKS

In this study, the bending deformation and transformation behavior of TRIP steel were investigated at various deflection rates through experiments and 3D-FE simulations. A fairly good agreement was observed between the computational and experimental results in both the quasi-static and impact conditions. Thus, the validity of the computation was confirmed. Then, the mechanism governing high energy absorption in TRIP steel was discussed based on the results of the computational prediction at room temperature and 80 K ($-193 \text{ }^\circ\text{C}$). The following conclusions can be drawn:

1. A positive rate sensitivity of the energy-absorption characteristic in TRIP steel can be observed from quasi-static to impact deformation. It is possible that TRIP steel possesses a better energy-absorption characteristic at higher deformation rate. At room temperature, the effect of SIMT on energy absorption in TRIP steel cannot be seen at high deformation rate at the investigated deflection. The mechanism of higher energy absorption at higher normalized deflection rate in TRIP steel can be explained from the viewpoint of rate sensitivity of strain hardening of austenite.
2. A concentration of high temperature rise is seen near the loading point in the impact deformation. The effect of high temperature rise on SIMT at high deflection rate is observed only in a small region. Moreover, the concentration of relatively temperature rise induces a localization of deformation near the loading point; however, this localization is retarded because of SIMT at low test temperature.
3. At low test temperature, the energy-absorption characteristic in TRIP steel is clearly improved by an increase in the strain hardening because of SIMT, especially at high deformation rate. In addition, at a high deflection rate, the ductility of TRIP steel is enhanced in three-point bending deformation because SIMT might delay the fracture that might occur near the loading point, leading an improvement of energy absorption.

ACKNOWLEDGMENT

We wish to thank Mr. Hashimoto of Webast Japan Corporation and Ms. Shi of Ondo Corporation for their assistance with the experimental investigations.

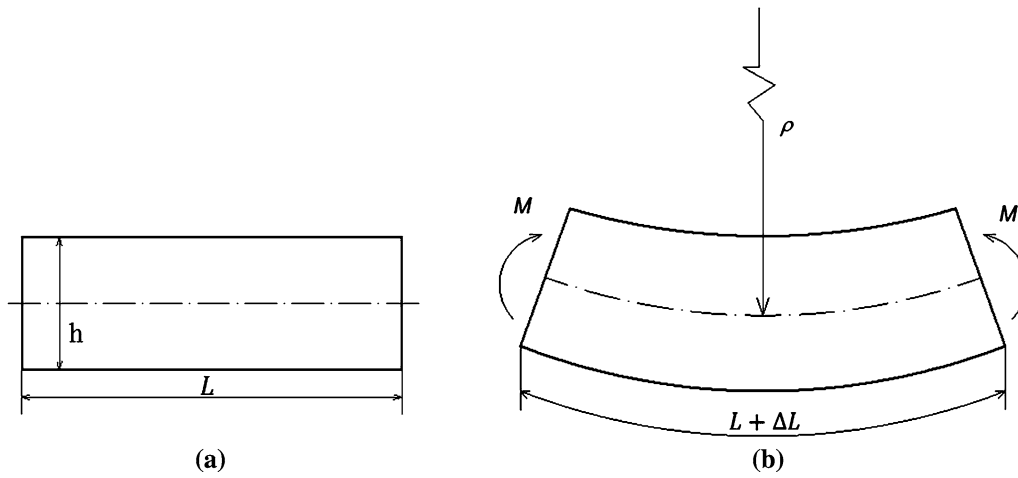


Fig. A1—The shape of the (a) un-deformed and (b) deformed beam.

APPENDIX A: DERIVATION OF EQ. [7]

The maximum bending strain in the case of small deformation is calculated in the case that the shape of the deformed specimen is assumed to be an arc as,

$$\delta_n = \varepsilon = \frac{\Delta L}{L} = \frac{h}{2\rho}, \quad [\text{A1}]$$

where ε is bending strain; L is span length; ΔL is the change in length at the lower surface of specimen, h is the height of specimen; ρ is radius of curvature as shown in Figure A1. With the curvature is assumed to be constant in the entire region of the deformed beam, ρ can be calculated as

$$\rho^2 = \left(\frac{L}{2}\right)^2 + (\rho - \delta)^2 \text{ and } \rho = \frac{L^2}{8\delta} + \frac{\delta}{2} = \frac{L^2}{8\delta} \{1 + 4(\delta/L)^2\}, \quad [\text{A2}]$$

where δ is the deflection. $(\delta/L)^2$ is considered to be quite small and can be neglected. Thus, we can obtain the following equation,

$$\rho = \frac{L^2}{8\delta}. \quad [\text{A3}]$$

From Eqs. [A1] and [A3], the normalized deflection is calculated as

$$\delta_n = \frac{h}{2L^2} \frac{8\delta}{L^2} = \frac{4h}{L^2} \delta. \quad [\text{A4}]$$

REFERENCES

1. F.D. Fischer, G. Reisner, E. Werner, K. Tanaka, G. Cailletaud, and T. Antretter: *Int. J. Plast.*, 2000, vol. 16, pp. 723–48.
2. T. Iwamoto, T. Tsuta, and Y. Tomita: *Int. J. Mech. Sci.*, 1998, vol. 40, pp. 173–82.
3. A. Khan, M. Baig, S. Choi, H. Yang, and X. Sun: *Int. J. Plast.*, 2012, vols. 30–31, pp. 1–17.
4. R. Mahnken, A. Schneidt, and T. Antretter: *Int. J. Plast.*, 2009, vol. 25, pp. 183–204.
5. A. Rusinek, J.A. Rodríguez-Martínez, R. Pesci, and J. Capelle: *J. Theor. Appl. Mech.*, 2010, vol. 48, pp. 1027–42.

6. I. Tamura: *Met. Sci.*, 1982, vol. 16, pp. 245–53.
7. Y. Tomita and T. Iwamoto: *Int. J. Mech. Sci.*, 1995, vol. 37, pp. 1295–1305.
8. R. Zaera, J.A. Rodríguez-Martínez, A. Casado, J. Fernández-Sáez, A. Rusinek, and R. Pesci: *Int. J. Plast.*, 2012, vol. 29, pp. 77–101.
9. R. Zaera, R.A. Rodríguez-Martínez, and D. Rittel: *Int. J. Plast.*, 2013, vol. 40, pp. 185–201.
10. H. Huh, S.B. Kim, J.H. Song, and J.H. Lim: *Int. J. Mech. Sci.*, 2008, vol. 50, pp. 918–31.
11. J. Huh, H. Huh, and C.S. Lee: *Int. J. Plast.*, 2013, vol. 44, pp. 23–46.
12. L. Durrenberger, D. Even, A. Molinari, and A. Rusinek: *J. Phys. IV.*, 2006, vol. 134, pp. 1287–93.
13. J.A. Nemes and J. Eftis: *Int. J. Plast.*, 1993, vol. 9, pp. 243–70.
14. T. Rong, L. Lin, B.C. De Cooman, W. Xi-chen, and S. Peng: *ISIJ Int.*, 2006, vol. 13, pp. 51–56.
15. S. Curtze, V.T. Kuokkala, M. Hokka, and P. Peura: *Mater. Sci. Eng. A*, 2009, vol. 507, pp. 124–31.
16. J.A. Rodríguez-Martínez, R. Pesci, and A. Rusinek: *Mater. Sci. Eng. A*, 2011, vol. 528, pp. 5974–82.
17. J.A. Rodríguez-Martínez, A. Rusinek, R. Pesci, and R. Zaera: *Int. J. Solids Struct.*, 2013, vol. 2, pp. 339–51.
18. R. Zaera, J.A. Rodríguez-Martínez, G. Vadillo, and J. Fernández-Sáez: *J. Mech. Phys. Solids*, 2014, vol. 64, pp. 316–37.
19. T. Iwamoto and T. Tsuta: *Int. J. Plast.*, 2002, vol. 18, pp. 1583–1606.
20. Y. Chuman, K. Minuras, K. Kaizu, and S. Tanimura: *Int. J. Impact Eng.*, 1997, vol. 19, pp. 165–74.
21. T. Yokoyama and K. Kishida: *Exp. Mech.*, 1989, vol. 29, pp. 188–94.
22. Y. Tomita and T. Iwamoto: *Int. J. Mech. Sci.*, 2001, vol. 43, pp. 2017–34.
23. G.B. Olson and M. Cohen: *Metall. Trans. A.*, 1975, vol. 6A, pp. 791–95.
24. R.G. Stringfellow, D.M. Parks, and G.B. Olson: *Acta Metall. Mater.*, 1992, vol. 40, pp. 1703–16.
25. T. Iwamoto, M. Cherkaoui, and T. Sawa: *Int. J. Mod. Phys. B*, 2008, vol. 22, pp. 5985–90.
26. T. Iwamoto and T. Tsuta: *Int. J. Plast.*, 2000, vol. 16, pp. 791–804.
27. T. Iwamoto, T. Kawagishi, T. Tsuta, and S. Morita: *JSME Int. J. Ser. A*, 2001, vol. 44, pp. 443–52.
28. T. Iwamoto: *Int. J. Plast.*, 2004, vol. 20, pp. 841–69.
29. T. Iwamoto and T. Tsuta: *Key Eng. Mater.*, 2004, vols. 274–276, pp. 679–84.
30. Y. Tomita and Y. Shibutani: *Int. J. Plast.*, 2000, vol. 16, pp. 769–89.
31. R.F. Kubler, M. Berveiller, and P. Buessler: *Int. J. Plast.*, 2011, vol. 27, pp. 299–327.
32. M. Fischlschweiger, G. Cailletaud, and T. Antretter: *Int. J. Plast.*, 2012, vol. 37, pp. 53–71.

33. D. Peirce, C.F. Shih, and A. Needleman: *Composite Struct.*, 1984, vol. 118, pp. 875–87.
34. J.D. Eshelby: *Proc. R. Soc. Lond.*, 1957, vol. A241, pp. 376–96.
35. J. Talonen: Effect of Strain-Induced α' -Martensite Transformation on Mechanical Properties of Metastable Austenitic Stainless Steels. Doctoral Dissertation, Helsinki University of Technology, 2007.